ZERO INSERTION FORCE MEMS SOCKET: 3D MULTI-CHIP ASSEMBLY FOR MICROROBOTICS

Hani C. Gomez, Craig B. Schindler, Harry L. Clark Jr, Joseph T. Greenspun, and Kristofer S. J. Pister*
Berkeley Sensor and Actuator Center
Department of Electrical Engineering and Computer Science
University of California, Berkeley

ABSTRACT

This paper presents an innovative approach for 3D multi-chip assembly using a zero insertion force (ZIF) MEMS socket, which was designed, fabricated and tested. We demonstrate: 1) 3D assembly between a ZIF socket and a linear MEMS motor, 2) 3D assembly between a socket and a microrobotic leg, and 3) resistance versus force data for probes coated with various metals, to characterize the electrical connections between the ZIF socket and the inserted chip. Potential applications for this work include microrobotics assembly (MEMS-MEMS) and probe cards for effortless testing of and 3D assembly with CMOS chips (MEMS-CMOS).

KEYWORDS

Microassembly, microrobot, microrobotics, 3D assembly, zero insertion force.

INTRODUCTION

In order to build microrobots, the goal of this project is to provide a streamlined microassembly solution to connect two chips together both mechanically and electrically. In the past, 3D assembly of MEMS chips has been conducted using wire bonding or silver epoxy [1]. Although they provide good electrical connections, wire bonders are time consuming, tedious, and not simple-to-use. Silver epoxy and/or solder can be messy and require additional lab work. Silver epoxy has also been speculated to contaminate the MEMS devices during the curing process, negatively affecting their performance. Furthermore, microgrippers and self-assembly are both not well developed, and come with disadvantages [2].

This work expands on a ZIF socket design presented at MARSS 2017 [3]. This previous work demonstrated the design of a latch, unlatch, clamp (labeled rigid pusher in [3]) and probes used for the ZIF socket. However, it never demonstrated the actuation of a MEMS motor or leg through the socket. It also reported high contact resistances in the 1-2kΩ range, which is higher than the desirable range for MEMS-CMOS assembly.

This paper also corrects the reported contact resistances of the ZIF socket, with values much lower than 1-2kΩ. It was observed that the MEMS chips used in [3] had a webbed film between the socket probes. When covered with metal, the film became conductive, therefore shorting out the probes. The high reported resistances were not contact resistances, but the resistance of the probes shorted by the now conductive thin film between them. To more accurately study the contact resistance of the socket, resistance vs force experiments are discussed in this paper.

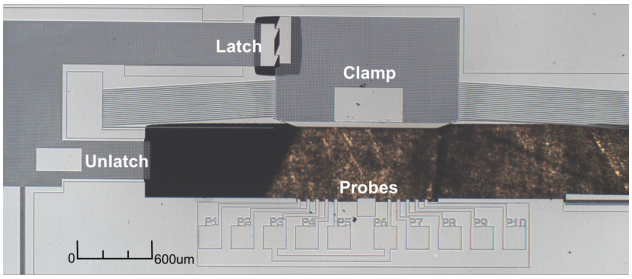

Figure 1: Microscope image of full ZIF socket design with latch engaged. The clamp has two latches to engage with, therefore reducing the overall strain on the latch and preventing any fractures.

SYSTEM DESIGN

All of the MEMS chips presented in this work were fabricated using a two-mask SOI process [1]. A design for the latch, unlatch, clamp (labeled rigid pusher in [3]) and probe designs can be seen in Fig. 1, where the latch is engaged.

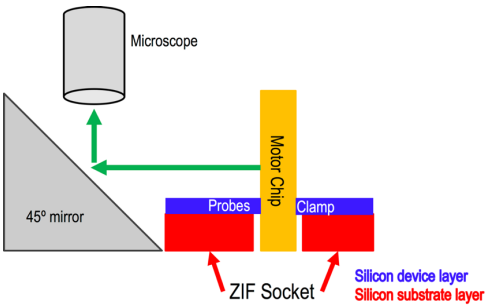

Figure 2: Test setup for an inserted MEMS linear motor chip in a ZIF socket. We observe the motor running through the 45° mirror.

Assembled Systems

Two assembled systems were designed and tested to investigate the functionality of the socket: a ZIF socket with a motor chip, and a ZIF socket with a leg chip. The assembly steps described in [3] were used to assemble the two systems. All inserted chips were tested and confirmed to be properly working prior to the assembly into the socket.

For our first test setup (Fig. 2), we assembled a motor chip similar to the design used in [4] into a ZIF socket. The ZIF socket had six probes designed to contact six pads on the motor chip. Post assembly, we used a 45° mirror to see the vertical chip moving through a microscope.

For the second test setup, we assembled a ZIF socket with a robotic leg (Fig. 3a) with linkage design similar to that presented at TRANSDUCERS 2017 [1]. Fig. 3b shows

a 3D CAD model of the assembled system, used to verify the dimensions of the ZIF socket and inserted chip before fabrication and assembly. A similar setup to that in Fig. 2 was used to confirm the connection between the leg chip and the socket.

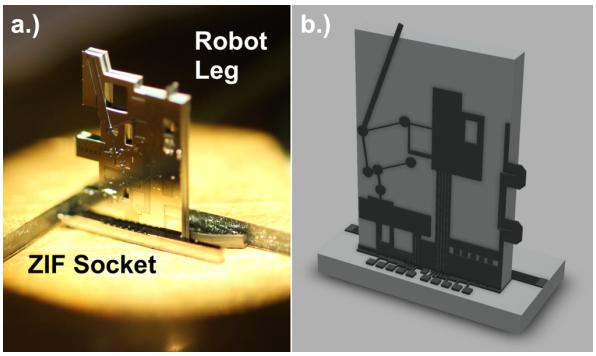

Figure 3: a.) A microrobot leg similar to the one presented in [4] assembled inside a ZIF socket. The leg is pointing up in this case. b.) A 3D model of the newest ZIF socket designs and robot leg chips seen in part a.).

Contact Resistance Characterization

Low contact resistances are desirable for MEMS-CMOS and MEMS-MEMS assemblies in order to improve the performance of the full system and reduce unnecessary parasitic resistances. To understand contact resistance, we start by observing one ZIF socket probe against one pad on the inserted chip. When the probes and pads are assembled, asperities (a-spots) on the surface of the connected ends will come into contact and eventually deform due to an applied force. Three regimes of contact can be observed: elastic, plastic, and compressive, where the contacts are covered by a residual, resistive film. Due to the higher forces (mN) used in this work, it is safe to assume the constriction resistance will not be in the elastic regime [5].

We can then model the plastic regime using Holm's classic theory [6]:

$$R_c = \frac{\rho}{2r} \tag{1}$$

$$A = \frac{F}{H} = \pi r^2 \tag{2}$$

Equation (1) assumes a circular contact area with radius r, and material resistivity ρ for both the probe and the pad. In the plastic regime, the contact area can be approximated by (2) to be equal to the applied load, F, of the contact divided by the material hardness, H [5,6]. Assuming a circular contact area, we can equate the two also in (2) [6,7]. Finally, (1) and (2) are used to derive the relationship between constriction resistance and a load contact force:

$$R_c = \frac{\rho}{2}\left(\frac{F}{H\pi}\right)^{-1/2} \tag{3}$$

It is important to note that (3) can be used in the compressive regime if the exponential of the force, F, is equal to -1 instead of -1/2. Although not as common in the literature, this regime can be used to explain higher resistances since it implies the tested contacts were contaminated with resistive films [6].

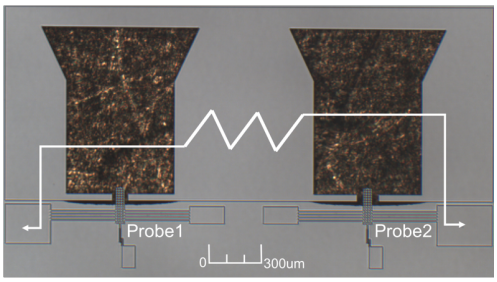

Figure 4: Microscope image of resistance versus force test structures used to characterize the electrical connections between the socket and the inserted chip.

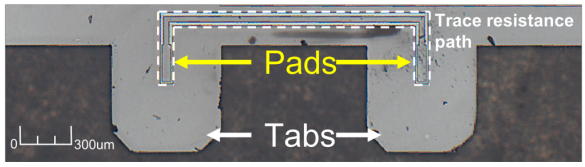

Figure 5: Inserted chip with a connected path used for resistance vs force measurements.

To experimentally obtain resistance versus force measurements, we designed a test structure, Fig. 4. Two probes are side by side, attached to clamped-clamped beams. To measure a resistance between them, we inserted a chip, Fig. 5, with connected pads on two side pillars into the test structure and pushed against it, taking multiple steps. At the opposite end of the probes in Fig. 4 are Vernier scales used to keep track of the total displacement, x, as the chip is pushed. Equation (4) is used to calculate the contact force, F at each step [3].

$$F(x) = \left(16\frac{Ew^3t}{L^3}x + 8\frac{Ewt}{L^3}x^3\right)N \tag{4}$$

To take resistance measurements, the inserted chip and test structure chip were 1) sputtered with Tungsten (W) and 2) evaporated with Gold (Au). The resistance was measured from probe 1 to probe 2 at each step. A similar test setup was used to obtain data for chips sputtered with Gold Palladium (AuPl), but using two probes attached to two beams in parallel. Figs. 6a and 6b show one single probe before and after engagement with the pads. Notice the reflection of the probe on the inserted, 90º vertical chip. To take the AuPd measurements, we used the actual ZIF socket probe design, which was less flexible than the test structures used for the Au and W measurements. Therefore, the force regime for the AuPd structures was much smaller.

Since the total resistance measured will not only include the constriction resistance, but also the trace resistances, an initial resistance was added to the analytical model. This initial resistance is assumed to be equivalent to the trace resistances in the test structures. We calculated the initial resistance using the measured sheet resistance of the metal films and the test structure geometries. Furthermore, to account for the two contacts from both probe 1 and 2, the constriction resistance was multiplied by 2. Our modified Holm's model is presented in (5).

$$R_{total} = R_{trace} + 2R_c \tag{5}$$

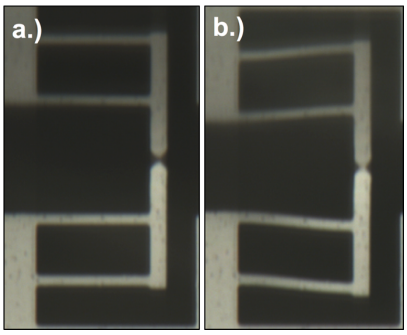

Figure 6: a.) & b.) Microscope image of the AuPl sputtered probes before and after engagement. Notice the reflection due to the orthogonal chip.

EXPERIMENTAL RESULTS

Assembly Systems

Implementing the test setup in Fig. 2, we actuated the linear motor with six probes on the ZIF socket connected to six pads on the motor test chip. Using the 45° mirror, the vertically standing, moving motor shuttle could be seen through the microscope, Fig. 7. The assembly in Fig. 3a was used in the setup from Fig. 2 to observe the actuated moving leg.

The probe to pad horizontal alignment precision achieved is ± 20 µm, and an SEM image of the misalignment can be seen in Fig. 8. The vertical alignment precision achieved is ±2µm.

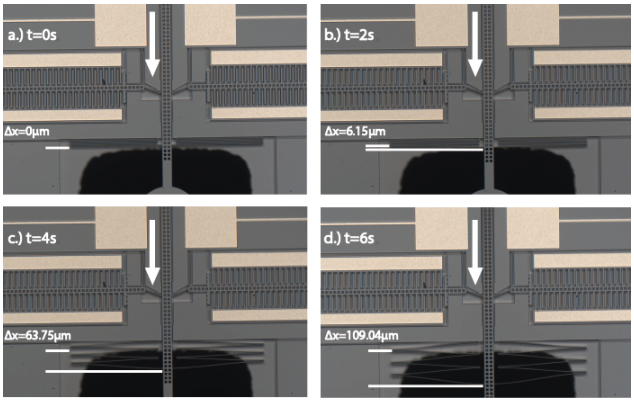

Figure 7: Snapshots of a video of the motor shuttle actuated through the ZIF socket. The measured times and shuttle displacements are noted.

Contact Resistance versus Force

Figs. 9, 10 and 11 show the resistance vs force plots for the Tungsten (W), Gold (Au) and Gold Palladium (AuPl) test structures, respectively. All resistance measurements were conducted using a Keithley 2634B Source Meter. The W structures were sputtered with 40nm of metal, and had a measured sheet resistance of 3.13 Ω/sqr. The Au structures were thermally evaporated with 100nm of the metal, and had a measured sheet resistance of 0.3Ω/sqr. A 5nm chrome film was used to adhere the Au to the Si chips. Its effect is disregarded in these calculations since it should have almost no effect on the resistance measurements. Finally, the AuPd structures were sputtered with 40nm of metal, and had a sheet resistance of 10Ω/sqr.

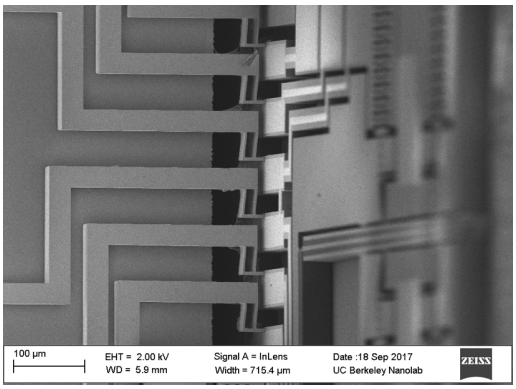

Figure 8: SEM image of the ZIF socket probes against the inserted chip pads, with a horizontal misalignment of 20µm.

Due to the difficulty in measuring thin film hardness, the hardness, H, of the films was approximated based on the literature. 25GPa, 2GPa, and 1GPa were used for the W, Au, and AuPd films respectively [5,7,8,9].

The measured resistance vs force lines are plotted against the modified Holm's model in (5), for the plastic regime. The sputtered W had a calculated trace resistance of 315Ω, and fits the plastic regime as expected. Post experimentation, it was noticeable that the probe scratched against the W pad (Fig. 12a). Fig. 12b shows a SEM image of the triangular probe tip covered with W on top. The scallops caused by DRIE in the fabrication process can be seen on the Si sidewalls. The evaporated Au had a calculated trace resistance of 30.3Ω. The total measured resistance was about 20Ω more than the model expected. A possible explanation is that Holm's model tends to underestimate the constriction resistance, as observed in the literature [7]. A lower range of forces could also be further studied for Au since it has a lower hardness value. A SEM image of the Au pad can be seen in Fig. 12c. The scratches were caused during insertion and testing of the chips. Finally, the sputtered AuPd had a calculated trace resistance of 320Ω, and is seen in Fig. 11. Only forces between 1-2mN were tested with the AuPd structures. It is possible that a higher range of forces needs to be tested to better fit the model.

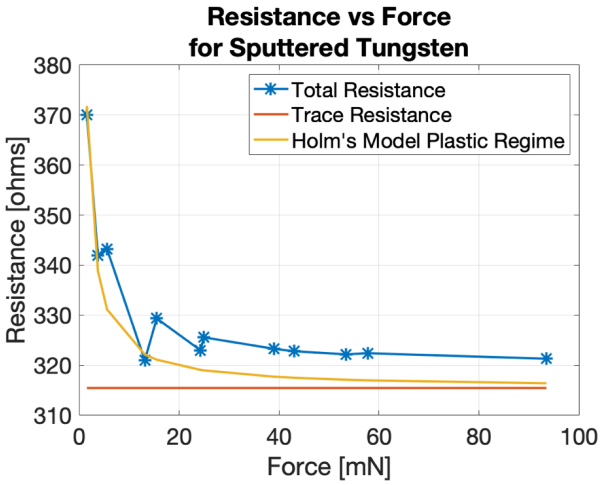

Figure 9: Plot of resistance vs force for Tungsten sputtered chips.

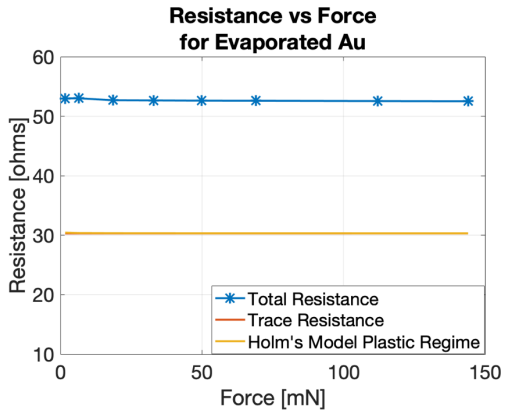

Figure 10: Plot of resistance vs force for Gold evaporated chips.

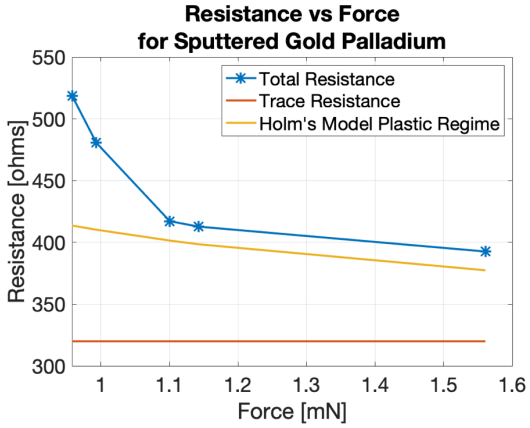

Figure 11: Plot of resistance vs force for AuPd sputtered chips.

CONCLUSIONS AND FUTURE WORK

An improved zero insertion force MEMS socket was fabricated based on the work in [3]. The socket was assembled both with a motor and a leg chip, confirming the successful electrical connection between the two chips by actuating the gap closing actuators on both inserted chips.

To characterize the socket, resistance vs force test structures were designed and fabricated. The expected constriction resistance was modeled using Holm's classic electric contact model [6], and plotted against the measured results. The sputtered W measurements lie closely to the plastic regime, while the evaporated Au film measured an additional parasitic resistance in comparison to the model predictions. We also hypothesize that the Au test structures studied too high a range of forces, while the AuPd sputtered test structures are probed too small a range of forces.

Future work involves the design of simpler resistance vs force test structure for a range of forces from 0-20mN, with a higher step count between each tested force. Various probe geometries will also be tested to determine the effect of probe geometry on the contact resistance.

To successfully achieve microrobotic assembly the ZIF socket design can be used to build a silicon walking microrobot. Four legs can be assembled to four ZIF sockets on a hub chip, and actuated through the main hub chip. This new assembly approach reduces the total number of wire bonds and assembly steps. Finally, a ZIF socket designed for assembly with a CMOS chip will be fabricated and tested. Implementing MEMS-CMOS multi-chip assembly would allow for a simpler and faster full-system integration of the walking microrobot.

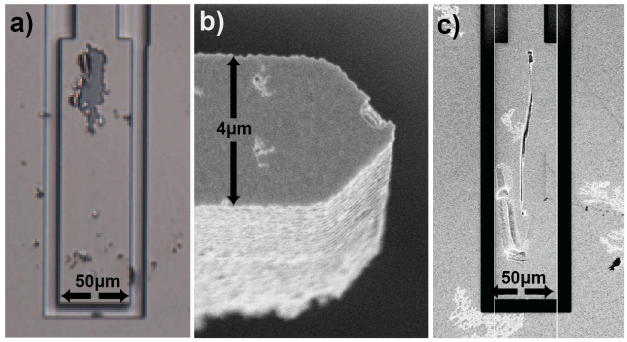

Figure 12: a) Microscope image of the Tungsten sputtered pad. The ZIF socket probe scratched against the pad. b) SEM image of the Tungsten covered triangular probe tip. c) SEM image of the Gold evaporated pad.

ACKNOWLEDGEMENTS

This work was financially supported by the National Science Foundation and the Berkeley Sensor & Actuator Center. All devices were fabricated and post-processed in the UC Berkeley Marvell Nanofabrication Laboratory.

REFERENCES

[1] D. S. Contreras, D. S. Drew, and K. S. Pister, "First steps of a millimeter-scale walking silicon robot," in Solid-State Sensors, Actuators and Microsystems (TRANSDUCERS), 2017 19th International Conference on, 2017, pp. 910–913.

[2] Bogue, Robert. "Assembly of 3D Micro---Components: a Review of Recent Research." Assembly Automation, vol. 31, no. 4, 2011, pp. 309–314.

[3] Gomez, H., et al. "Zero Insertion Force MEMS Socket for Microrobotics Assembly." MARSS 2017

[4] Penskiy, I., et al. Optimized Electrostatic Inchworm Motors using a Flexible Driving Arm., Journal of Micromechanics and Microengineering, 2013.

[5] G.M. Rebeiz, RF MEMS: theory, design, and technology. John Wiley& Sons, 2004.

[6] R. Holm, Electric contacts: theory and application. Springer Science& Business Media, 2013.

[7] M. Read, J. Lang, A. Slocum, and R. Martens, "Contact resistance in flat thin films." Institute of Electrical and Electronics Engineers, 2009.

[8] H. Sun, Z. Song, D. Guo, F. Ma, and K. Xu, "Microstructure and mechanical properties of nanocrystalline tungsten thin films," Journal of Materials Science & Technology, vol. 26, no. 1, pp. 87–92, 2010.

[9] Wen, Q. Meng, W. Yu, W. Zheng, S. Mao, and M. Hua, "Growth, stress and hardness of reactively sputtered tungsten nitride thin films," Surface and Coatings Technology, vol. 205, no. 7, pp. 1953–1961, 2010.

CONTACT

*Hani C. Gomez; gomezhc@berkeley.edu